remote sensing

MDPI

Article

Statistics of Smoke Sphericity and Optical Properties Using Spaceborne Lidar Measurements

Natalie Midzak [1,*], John E. Yorks [2] and Jianglong Zhang [3]

[1] NASA Postdoctoral Program Fellow, NASA Goddard Space Flight Center, Greenbelt, MD 20771, USA
[2] NASA Goddard Space Flight Center, Greenbelt, MD 20771, USA; john.e.yorks@nasa.gov
[3] Department of Atmospheric Sciences, University of North Dakota, Grand Forks, ND 58202, USA; jianglong.zhang@und.edu
* Correspondence: natalie.midzak@nasa.gov

Abstract: Smoke particles from biomass burning events are typically assumed to be spherical despite previous observations of non-spherical smoke. As such, large uncertainties exist in some physical and optical parameters used in lidar aerosol retrievals, including depolarization and lidar ratio of non-spherical smoke aerosols. In this analysis, using NASA's Cloud-Aerosol Lidar with Orthogonal Polarization (CALIOP) data during the biomass burning season over Africa from 2015 to 2017, we studied the frequency and distribution of non-spherical smoke particles to compare with findings of smoke particle non-sphericity from the Cloud-Aerosol Transport System (CATS) lidar. A supplemental smoke aerosol typing algorithm was developed to identify aerosol layers containing non-spherical smoke particles, which might otherwise be misclassified as desert dust, polluted dust, or dusty marine by the CALIOP standard aerosol typing algorithm. Then, the relationships between smoke particle sphericity, lidar ratio, and relative humidity are analyzed for CATS and CALIOP observations over Africa. Approximately 18% of smoke layers observed by CALIOP over Africa are non-spherical (depolarization ratio > 0.075) and agree with spatial distributions of non-spherical smoke found in CATS observations. A dependance of lidar ratio on relative humidity was found for layers of spherical smoke over Africa in both CATS and CALIOP data; however, no such dependance was evident for the depolarization ratio and layer relative humidity. While the supplemental smoke aerosol typing algorithm presented in this analysis was targeted only for specific biomass burning regions during biomass burning seasons and is not meant for global operational use, it presents one potential method for improved backscatter lidar aerosol typing. These results suggest that a dynamic lidar ratio, based on layer-relative humidity for spherical smoke, could be used to reduce uncertainties in smoke aerosol extinction retrievals for future backscatter lidars.

Keywords: lidar; smoke aerosols; biomass burning

Academic Editor: Pavel Kishcha

Received: 29 November 2024
Revised: 10 January 2025
Accepted: 12 January 2025
Published: 25 January 2025

Citation: Midzak, N.; Yorks, J.E.; Zhang, J. Statistics of Smoke Sphericity and Optical Properties Using Spaceborne Lidar Measurements. *Remote Sens.* **2025**, *17*, 409. https://doi.org/10.3390/rs17030409

1. Introduction

Annual biomass burning occurs throughout much of the globe and is a primary contributor of anthropogenic aerosol emissions that have major direct and indirect effects on the Earth's climate and can negatively affect local air quality and visibility [1]. Accurate knowledge of the vertical distribution of aerosol optical properties, such as aerosol extinction, are equally important for a variety of aerosol-related applications, including the study of aerosol and cloud interactions [2]. Therefore, through retrieving vertical information of attenuated backscatter, depolarization ratio, optical depth, and extinction profiles, lidar serves as a strong tool to study the physical and optical characteristics of aerosol particles

such as smoke aerosols from wildfires and biomass burning. Observations from spaceborne backscatter lidar instruments such as the Cloud-Aerosol Transport System (CATS) and Cloud-Aerosol Lidar with Orthogonal Polarization (CALIOP) have been extensively used for monitoring of spatial–temporal variations in atmospheric aerosol optical properties. Still, large uncertainties exist in some physical and optical parameters used in lidar aerosol retrievals, including depolarization and lidar ratio.

Aerosol extinction for a given layer, using measurements from a backscatter lidar, is related to range-resolved backscattered averaged signal [3] using the extinction-to-backscatter ratio, or the lidar ratio, through an iterative process [4,5]. The lidar ratio is assumed to be constant for a specified layer type; thus, accurate detection of atmospheric aerosol layers is required to obtain the most appropriate extinction coefficient values [6]. Yet, the lidar ratio can vary significantly as functions of observing conditions and aerosol types and remains one of the largest uncertainty sources for backscattered lidar aerosol retrievals from both CATS [7,8] and CALIOP [9,10]. Therefore, careful atmospheric aerosol layer typing (and hence accurate lidar ratio assignment) is needed for the most accurate aerosol extinction retrievals. The most common retrieval technique for CATS and CALIOP is to assume a default lidar ratio. For CATS aerosol layers, a look-up table following the values used in the Geosciences Laser Altimeter System (GLAS), Cloud Physics Lidar (CPL) and CALIPSO algorithms [11,12] is used to assign a value of layer lidar ratio based on layer type. For example, currently, the empirically derived value of the 1064 nm lidar ratio for all smoke plumes is set as 40 sr for CATS retrievals and 30 sr for CALIOP (70 at 532 nm).

Backscatter lidar aerosol typing algorithms rely heavily on feature-integrated depolarization ratio threshold values to discriminate between aerosol species, and smoke particles are generally assumed to be spherical in those aerosol typing algorithms [13,14]. Clearly, misclassifications by aerosol typing algorithms may lead to inaccurate lidar ratio assignments. Yet, both observational-based studies (e.g., [15–17]) and theoretical analyses [18–20] suggest the presence of non-spherical smoke particles, which may be misclassified as non-smoke aerosols by the lidar aerosol typing algorithms. Further complicating smoke aerosol depolarization retrievals is the impacts of aging on their microphysical properties. For example, smoke particle depolarization ratios can decrease within ~1–2 weeks after their release and continue to undergo modifications depending on their duration in the troposphere, vertical distribution, and atmospheric meteorological conditions. In cases of extreme fire events, smoke particles may overshoot the tropopause and enter the stratosphere, where non-spherical particles have much longer residence times [21–24]. Thus, uncertainties in retrieved aerosol extinctions are to be expected by assigning non-smoke aerosol lidar ratios to those non-spherical smoke aerosol layers.

In a recent study, Midzak et al. (2023) [17] apply a modified smoke aerosol typing algorithm to identify layers of non-spherical smoke over southern Africa and South America using CATS 1064 nm volume depolarization ratio (VDR) retrievals. The layer-integrated VDR is defined as the ratio between the feature-integrated perpendicular attenuated (molecular plus particulate) backscatter to the parallel attenuated backscatter signal (detailed in Section 2.1). The modified smoke typing algorithm presented by Midzak et al. (2023) [17] was applied only over known biomass burning regions during the peak biomass burning season and not intended for global operational use as it implements validation efforts relying on AErosol RObotic NETwork (AERONET) and National Center for Environmental Prediction (NCEP)/National Center for Atmospheric Research (NCAR) Reanalysis data and may still include dust contamination in the non-spherical smoke analysis. Although only 3 years of biomass burning observations are available at 1064 nm as part of the CATS dataset, Midzak et al. (2023) [17] suggest that, in general, smoke layers with increased

values of VDR are produced from the burning of vegetation in dry regions, while spherical smoke layers with lower VDR result from regions of increased soil moisture.

In Midzak et al. (2023) [17], the spatial distributions of spherical and non-spherical smoke aerosols were estimated over southern Africa and South America using lidar observations from CATS. It is thus interesting to apply a similar approach to lidar observations from CALIOP and intercompare detected non-spherical smoke aerosol regions/seasons from both instruments. Note that while 1064 nm VDR data were used in Midzak et al. (2023) [17] to classify non-spherical smoke aerosol layers, only the 532 nm particulate depolarization ratio is available in the CALIOP dataset. However, because the particulate contribution to the backscattered signal is significantly higher at 1064 nm than 532 nm, the CATS 1064 nm VDR and CALIOP 532 nm particulate depolarization are assumed to provide the same information [25]. This assumption is implemented in the analysis of Kar et al. (2018) [25] and used in this analysis as well.

In addition, while the current CATS retrieval method relies on a prebuilt look-up table for lidar ratio as a function of aerosol type, throughout the years, various methods have also been developed to constrain estimates of layer-averaged lidar ratio, including the transmission loss constrained method [26] and the constrained lidar ratio over the opaque water cloud method [27]. Utilizing those lidar ratio retrieval methods, in conjunction with the smoke aerosol sphericity detection method developed by Midzak et al. (2023) [17], it is also feasible to study the difference in lidar ratios between spherical and non-spherical smoke aerosols and further explore the differences as a function of observing conditions.

Therefore, this study investigates the distribution of non-spherical smoke identified in CALIOP lidar observations over southern Africa from biomass burning during 2015–2017 for comparison with the smoke frequencies and spatial distribution from CATS observations presented in Midzak et al. (2023) [17]. Additionally, relationships between the smoke aerosol lidar ratio and layer relative humidity from CATS and CALIOP are analyzed for all smoke layers observed by the sensors. Lidar ratio remains one of the largest sources of uncertainty for AOD retrievals from backscatter lidars; thus, these results have important implications for accurate retrievals of smoke aerosol lidar ratio values in the future. In this paper, we highlight findings of non-spherical smoke aerosol layers from CALIOP observations and present the relationship between lidar ratio and relative humidity. In addition, we build on the results of Midzak et al. (2023) [17] by applying their methodology for non-spherical smoke aerosol detection over Africa. This analysis relies on CALIPSO 532 nm retrievals to study if trends in non-spherical smoke frequency and spatial distribution are consistent between sensors. Then, the relationships between smoke particle sphericity, lidar ratio, and relative humidity are analyzed for CATS and CALIOP observations over Africa.

In this paper, the data and methodology used for the analysis are presented in Section 2. This Section also describes the theory of aerosol above-cloud retrievals which are applied in the lidar data. Section 3 presents the results of this analysis, while Section 4 provides their impacts on backscatter lidar extinction retrievals and a summary of previous studies which have focused on the relationship between lidar ratio and relative humidity. Finally, a summary of this analysis and conclusions are presented in Section 5.

2. Data and Methodology

2.1. Cloud-Aerosol Transport System

CATS [28] is a standard backscatter lidar that operated onboard the International Space Station (ISS) from February 2015 to October 2017. The unique 51-degree ISS inclination enabled characterization of the diurnal variation in clouds and aerosols. CATS primarily operated in Mode 7.2 utilizing the 1064 nm wavelength for total attenuated backscatter measurements and VDR measurements [28]. The layer-integrated VDR can be useful for

cloud phase and aerosol typing. Pulsed laser systems, such as those used in the CATS instrument, naturally produce linearly polarized light. Therefore, a beam splitter in the receiver optics system is used to separate the perpendicular and parallel polarized return signal to enable estimates of the VDR [29]. While spherical particles have VDR near zero, increasing VDR values indicate increasing non-sphericity. A large source of uncertainty in the VDR is the random error from solar background noise. During the daytime, this uncertainty is compounded by the fact that the solar background noise is higher in both the parallel and perpendicular channels. As such, only nighttime data are used in this analysis.

CATS Mode 7.2 Version 3.00 Level 1B (L1B) products such as profiles of total attenuated backscatter and VDR are reported at 60 m vertical and 350 m horizontal resolutions, while Level 2 (L2) products, such as aerosol extinction profiles, are reported at 60 m vertical and 5 km horizontal resolutions [30]. The CATS data products also include profiles of relative humidity reported to match the standard Level 2 profile resolution of 5 km horizontal and 60 m vertical. These data are interpolated from ancillary meteorological data provided by Modern-Era Retrospective Analysis for Research and Applications (MERRA-2). Uncertainty in the MERRA-2 relative humidity data was analyzed by Lou et al. (2020) [31] who reported averaged relative humidity differences between MERRA-2 and radiosonde data are within 10%; however, this value was dependent on latitude and altitude. Differences as high as 60% were reported near the African coast below 800 mb near the edges of dust aerosol plumes (Lou et al., 2020) [31], which may contribute to the variability in the results presented in this analysis.

2.2. Cloud-Aerosol Lidar with Orthogonal Polarization

The CALIOP instrument flew on board the Cloud-Aerosol Lidar and Infrared Pathfinder Satellite Observations (CALIPSO) satellite as part of the A-train constellation for nearly two decades (2006–2023), providing multiwavelength daily global coverage of clouds and aerosols from a 705 km sun-synchronous polar orbit [32]. The horizontal resolution of the Version 4 (V4) Level 2 (L2) data products is 5 km with a vertical resolution between 30 and 60 m from the surface up to 20 km. Additionally, vertical profiles of attenuated total backscatter (ATB) are reported at 532 and 1064 nm, while volume and particulate depolarization ratio products are provided at 532 nm. This is unlike CATS, which reports VDR at 1064 nm. However, because the particulate contribution to the backscattered signal is significantly higher at 1064 nm than 532 nm, the CATS 1064 nm VDR and CALIOP 532 nm particulate depolarization are assumed to provide the same information [25]. This assumption is implemented in the analysis of Kar et al. (2018) [25] and used in this analysis as well. Similarly to the CATS data, solar background noise in the CALIOP retrievals is higher during the day; therefore, only CALIOP nighttime data are used in this analysis.

The CALIPSO V4 aerosol subtype selection scheme for tropospheric aerosols combines polluted continental and smoke aerosol types into a single category. Polluted continental/smoke aerosols are those identified by CALIOP with particulate depolarization ratio values less than 0.075, total attenuated backscatter greater than 0.0005 and layer top heights less than 2.5 km. If the layer top heights are greater than 2.5 km, however, the features are classified as elevated smoke layers in the V4 scheme. The integrated particulate color ratio (χ'), the ratio of 1064 nm backscatter to 532 nm backscatter, is reported in CALIOP L2 data and can be used as an indicator of particle size. While small particles (e.g., smoke and polluted continental aerosols) exhibit a broad peak around 0.5, larger particles such as dust will have a peak closer to 0.7 [25]. In general, uncertainties in the particulate color ratio are in the order of 150–200% [25]. The CALIOP dataset also includes relative humidity data interpolated from MERRA-2. As noted above, these data are found to generally agree well with radiosonde data [33] and are used in this analysis.

2.3. Identification of Non-Spherical Smoke Regions Using CALIOP Data

In this analysis, smoke aerosols from biomass burning over southern Africa were separated into spherical and non-spherical smoke layers following the methodology detailed in Midzak et al. (2023) [17]. In Midzak et al. (2023) [17], aerosol layers identified as smoke following the standard aerosol typing algorithm were included in the analysis. Additionally, non-smoke aerosol layers over biomass burning regions during the biomass burning season with a layer thickness >0.5 km and 1064 nm VDR > 0.1 were classified as potential non-spherical smoke candidates. Then, NCEP/NCAR Reanalysis wind speed data were analyzed to exclude potential dust contamination. The NCEP/NCAR Reanalysis project provides a long-term global record of atmospheric variables including surface, 700 and 850 mb winds [34]. Upon classifying non-spherical smoke layers, an extensive validation effort was conducted which studied HYSPLIT back trajectories from several dozen cases to confirm that the source regions of non-spherical smoke layers were not desert regions. Data from AERONET stations collocated with non-spherical smoke layers were analyzed for Angstrom exponent, AOD, fine mode fraction and the imaginary part of the refractive index to confirm the presence of smoke. The global network of AERONET sun/sky radiometers provides long-term AOD measurements at wavelengths ranging from 340 to 1640 nm [35]. The spectral dependence of AOD with the wavelength, also called the Angstrom exponent, is retrieved at a range between 440 and 870 nm with low values (<1.0), indicating the presence of coarse mode aerosol and larger values (>1.5) measuring the presence of fine mode aerosol such as smoke [36–39]. This modified algorithm applied in Midzak et al. (2023) [17] found that up to ~15% of aerosol layers were misclassified by the standard typing algorithm, thus leading to inaccuracies in the lidar ratio assignments and extinction retrievals for these smoke aerosols.

The modified smoke typing algorithm adapted from Midzak et al. (2023) [17] was applied over southern Africa to identify the frequency and distribution of non-spherical smoke layers observed by CALIOP. This modified algorithm relies on a 532 nm layer-integrated particulate depolarization ratio threshold value of 0.075 to separate the spherical smoke aerosol from non-spherical smoke aerosol layers based on the findings of Kim et al. (2018) [13] and Tackett et al. (2023) [40]. The integrated particulate depolarization ratio from CALIOP represents the contribution by aerosol particles to the volume depolarization ratio within the layer. It is calculated by taking the ratio of the perpendicular polarized backscattered signal to the parallel polarized backscattered signal integrated from the base altitude to the top altitude of an identified atmospheric feature. [13,25,32,33,40]. Layer-integrated VDR captures an integrated value of depolarization, while a value of depolarization at a particular altitude describes only depolarization at one level, as is shown in Kar et al. (2018) [25]. Only the nights that met the validation criteria and were used in Midzak et al. (2023) [17] were included in this analysis to keep datasets comparable between the two studies. These criteria included westerly or southwesterly surface winds < 2 m/s from the Namib or Kalahari desert regions and 1064 nm AOD > 0.05 to eliminate background aerosol layers.

Similarly to the CATS aerosol typing algorithm, CALIOP relies on a threshold-based method to distinguish between aerosol types (Kim et al., 2018) [13], which may introduce the possibility of aerosol misclassifications. In the original CALIOP V4 aerosol subtype scheme, aerosols with feature-integrated 532 nm particulate depolarization ratio >0.075 are classified as desert dust, polluted dust or dusty marine depending on their depolarization ratio, altitude and the underlying surface [13]. However, Kim et al. (2018) [13] and Tackett et al. (2023) [40] note the occurrence of depolarizing smoke in the troposphere and recognize aerosol misclassifications of non-spherical smoke due to the depolarization ratio threshold implemented in aerosol classification. Since CALIOP reports particulate depolarization ratio values at 532 nm, unlike 1064 nm used in CATS, the threshold used for

smoke particle sphericity was updated from the values used in Midzak et al. (2023) [17] to account for the difference in wavelength. While a 1064 nm VDR value of 0.10 is used to separate between spherical and non-spherical smoke in the CATS aerosol layers, depolarizing smoke was estimated as having layer-integrated 532 nm particulate depolarization ratio values between 0.075 and 0.20 in the CALIOP dataset [12]. Therefore, a value of 0.075 is the threshold applied to the 532 nm CALIOP particulate depolarization observations to separate spherical and non-spherical smoke aerosols in this analysis.

Applying these criteria and the new layer-integrated depolarization ratio threshold to the CALIOP data during the peak biomass burning season (July–October) of 2015, 2016 and 2017, approximately 18% of identified smoke aerosol layers were found to be non-spherical with layer-integrated particulate depolarization ratio values >0.075.

2.4. Constrained Lidar Ratio Calculations for Smoke Layers

Due to the nature of backscatter lidar retrievals, a direct calculation of the layer lidar ratio is not always possible, and often the value of lidar ratio is assigned to an atmospheric layer based on layer type [11,12,41]. However, Hu et al. (2007) [27] present a method for determining the lidar ratio using opaque water clouds as a constraint for the retrieval. This lidar ratio retrieval technique has been used previously on space-based lidar data from CALIOP [27,42] and was implemented as part of the CATS V3 data release to constrain the lidar ratio for cirrus clouds and aerosol layers above opaque liquid water clouds, resulting in more accurate lidar ratio retrievals than an assigned default value based on the feature type. The aerosol above-cloud lidar ratio method, also referred to as the opaque constrained method, is applied in this analysis to both CATS and CALIOP spherical smoke aerosol layers from African biomass burning during the 2015–2017 biomass burning seasons. This method of lidar ratio calculation was evaluated by Liu et al. (2015) [42] over the western coast of Africa and the eastern Atlantic Ocean. They found mean values for smoke retrievals over this region of 70.8 sr. This value aligns well with our analysis, which found a mean smoke aerosol lidar ratio of 71 sr using the opaque constrained technique over the same geographic region.

Additionally, available AERONET AOD values were used to constrain the lidar ratio calculation for both CATS and CALIOP smoke layers over Africa. In this method, the independent collocated value of AOD is used to constrain the lidar ratio calculation following Fernald et al. (1972) [43] and several other authors [44–46]. This constrained method of lidar ratio calculation is preferred to assigning a default layer-averaged lidar ratio based on a look-up table as it is more accurate to the specific smoke aerosol layer. The aerosol lidar extinction profiles/lidar ratios derived from this method are used as the "true aerosol extinction profiles/lidar ratios" in this study to evaluate lidar aerosol extinction profiles from other methods.

3. Results

3.1. Observations of Non-Sphrical Smoke Using CALIOP

Figure 1 shows regions of spherical (left) and non-spherical (right) smoke layers identified in the CALIOP data over central and southern Africa during the 2015–2017 biomass burning seasons. Spherical smoke layers with layer-integrated depolarization ratio values <0.075 are highly concentrated closer to the equator between 0° and 20°S. An additional area with a high frequency of spherical smoke aerosols is present off the western coast of Africa and eastern Atlantic Ocean centered around 10°S. The mean and median of the CALIOP layer-integrated particulate depolarization values of spherical smoke are 0.03. These results are consistent with those of Midzak et al. (2023) [17], who note the presence

of spherical smoke layers in these same regions that comprise evergreen and deciduous forests with higher values of soil moisture.

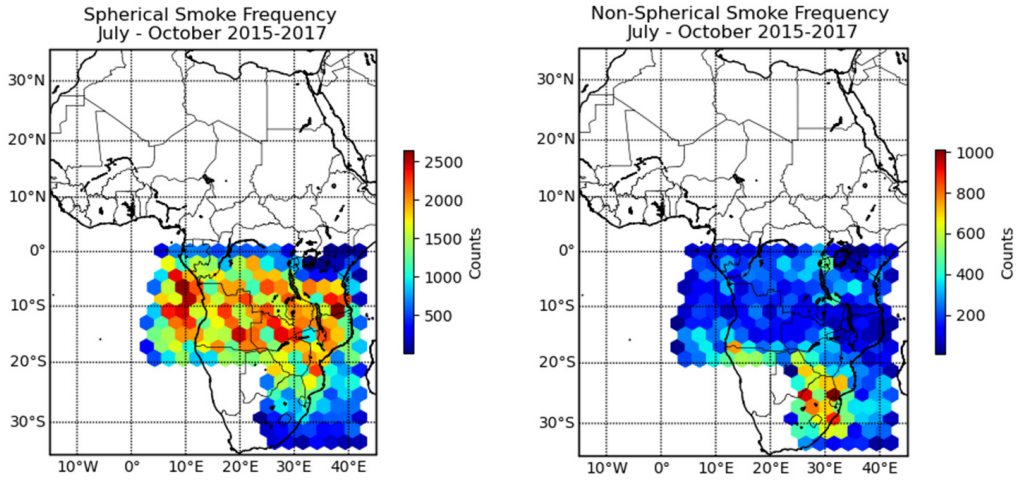

Figure 1. The spatial distribution of spherical (**left**) and non-spherical (**right)**) smoke aerosol layers identified by Cloud-Aerosol Lidar with Orthogonal Polarization (CALIOP) over Africa during the biomass burning season (2015–2017) using the supplemental aerosol typing algorithm. Spherical smoke layers (**left**) are centered closer to the equator, while non-spherical smoke layers (**right**) are located in the southern portion of the continent.

Conversely, non-spherical smoke aerosol layers with layer-integrated particulate depolarization ratio values >0.075 are presented in Figure 1 (right). These layers have a mean 532 nm layer-integrated particulate depolarization ratio of 0.20 and a median of 0.11. To minimize the potential for a high bias in the depolarization ratio due to dust contamination, regions of south-western Africa containing the Namib or Kalahari deserts are excluded from the analysis. Non-spherical smoke layers (Figure 1, right) are concentrated primarily poleward of 20°S, further south than their spherical counterparts. These regions predominantly comprise dry grasslands with lower values of soil moisture than northern regions [17]. High frequencies of non-spherical smoke layers are also identified near the equator between 30° and 40°E, consistent with the findings of Midzak et al. (2023) [17]. This region is made up of grasslands, which is consistent with the biome of non-spherical smoke particles to the south. The spatial distributions of CALIOP non-spherical smoke aerosol layers presented in Figure 1 support those presented in Midzak et al. (2023) [17], which hypothesizes that non-spherical smoke layers originate from a region of dry vegetation with lower soil moisture values, while spherical layers are from a moist burning region. One notable difference between Figure 1 and the results of Midzak et al. (2023) [17] is the frequency of non-spherical smoke in the northeastern corner of the African domain centered around Lake Victoria (0–5°S and 30–40°E). The smoke and dust production in this region is highly variable and a close examination of data from the AERONET site located at 0.4°S, 34.2°E was conducted in this study. Only days within the study period which had Angstrom exponents >1.5 and fine mode fraction >0.7 indicating the presence of smoke were retained in this analysis of CALIOP data; however, this methodology was not in place for the analysis conducted by Midzak et al. (2023) [17].

Smoke layers over central and southern Africa from August 2006 to 2010 were examined by Kar et al. (2018) [25], who note the transport of smoke aerosol layers from the western coast of Africa over the eastern Atlantic Ocean. Kar et al. (2018) [25] presented evidence of smoke particle growth by examining CALIOP χ' and link increased χ' with smoke particle swelling by uptake of water. Figure 2 shows CALIOP median values of χ' over central and southern Africa during the analysis period of this study (July–September

2015–2017). Each 1.5 by 1.5-degree bin contains at least 250 observations of smoke aerosol χ' from smoke layers identified using the supplemental smoke aerosol typing algorithm adapted from Midzak et al. (2023) [17]. Regions over central Africa display lower values of χ' centered around 0.5, while values over water approach χ' of 0.8. This indicates the presence of smaller particles over the continent and larger values over the ocean, similar to results presented by Kar et al. (2018) [25]. The median layer-integrated color ratios of spherical (0.58) and non-spherical (0.73) smoke suggest that the latter layers may consist of slightly larger particles, but plots of layer-integrated color ratios vs. layer-integrated depolarization ratios for all smoke layers did not show a statistically significant trend. An analogous comparison of smoke χ' from CATS, however, is not available as CATS primarily relied on 1064 nm backscatter measurements for retrievals.

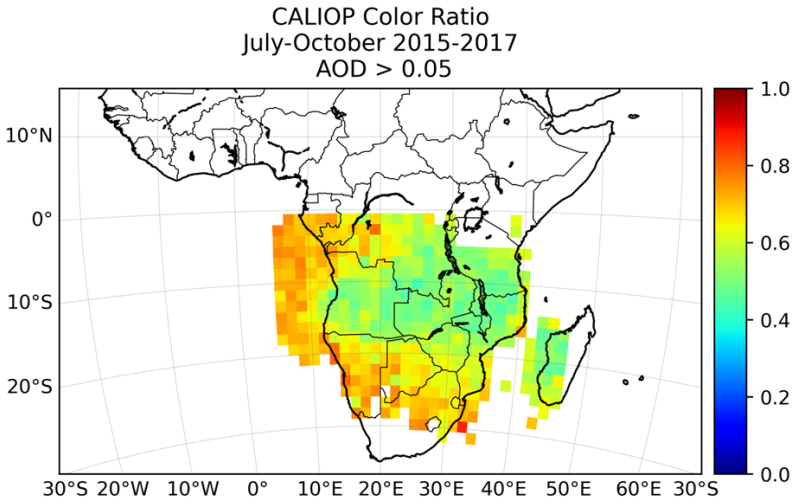

Figure 2. Color ratio values for all smoke aerosol layers identified by CALIOP with >250 observations per each 1.5 by 1.5-degree bin.

In addition to CALIOP χ', Kar et al. (2018) [25] examined the 532 nm depolarization ratio values of CALIOP and 1064 nm CATS depolarization ratio data of biomass burning plumes over southern Africa from August 2015 to 2016. Despite the differences in wavelengths of depolarization retrievals between the sensors, general trends of increasing depolarization ratio over the southern portion of the continent are evident. Figure 3 shows the median 532 nm layer-integrated particulate depolarization ratio from CALIOP in 1.5 by 1.5-degree bins each containing at least 250 observations of smoke aerosol. Generally, lower values of depolarization are found toward the equator in the region of spherical smoke observations discussed previously, while larger values of depolarization ratio are further south where non-spherical smoke was documented. The results of spherical smoke presented in Figure 3 are consistent with smoke identified in the CALIPSO typing algorithm; however, the non-spherical smoke layers are new smoke detections that the standard CALIPSO aerosol typing algorithm would misclassify as a dust-type aerosol. The results presented in Figure 3 are consistent with those of Kar et al. (2018) [25] and align with non-spherical smoke observations from other space-based lidar sensors (Midzak et al., 2023) [17], which highlights the persistence of these trends over the annual biomass burning season and are not limited to the August 2015–2016 analysis period used in Kar et al. (2018) [25].

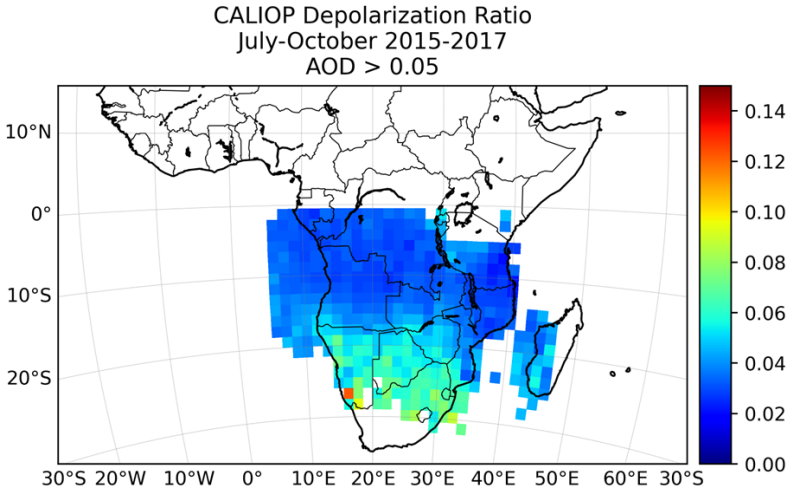

Figure 3. Particulate depolarization ratio values for all smoke aerosol layers identified by CALIOP with >250 observations per each 1.5 by 1.5-degree bin.

3.2. Dependence of Smoke Aerosol Lidar Ratio on Depolarization Using CATS and CALIOP Observations

The aerosol above-cloud method for constraining the lidar ratio (Hu et al., 2007) [27] and AERONET constrained method described previously were analyzed for smoke plumes identified by CATS and CALIOP over southern Africa during July–September 2016–2017. This period was chosen to reduce the chance of dust contamination and to align with AERONET operations over the selected domain. Although the AERONET AOD value as a constraint is the preferred method for the lidar ratio calculation, AERONET data were not continuously available during the analysis period. Therefore, a combination of the opaque constrained method (Hu et al., 2007) [27] and the AERONET constrained method are presented. Because of the requirement of an opaque liquid water cloud below the transparent smoke plume that is intrinsic to this method, the majority of lidar ratio retrievals using the aerosol above-cloud constrained approach are located near the southeastern Atlantic Ocean where there are persistent smoke plumes above stratocumulus cloud decks [47,48]. Smoke plumes in this region have been the target of major field studies including the Southern African Regional Science Initiative (SAFARI; Swap et al., 2002) [49] and the ObseRvations of Aerosols above Clouds and their intEractionS (ORACLES; Zuidema et al., 2016) [50] campaigns.

Figure 4 (left) shows the mean CATS 1064 nm constrained lidar ratio for non-spherical smoke aerosol plumes as a function of VDR $\pm$ 1 standard deviation for two years (2016–2017) of biomass burning seasons (July–September) over Africa. Both constrained methods provide similar results and dependencies and are therefore combined in this analysis. Only observations within 10 degrees of an operational AERONET station within a 5°S–25°S and 2°E–22°E grid box were reported. Only days with NCEP/NCAR Reanalysis data indicating easterly 850 mb winds over the region were used in this analysis. This is the dominant wind pattern over this region as prevailing winds usher smoke aerosol from southern Africa over the Atlantic Ocean during the biomass burning months [51]. Further, only observations with an AERONET-reported Ångström exponent $\geq$ 1.5 and fine mode fraction $\geq$ 0.7 for the day of, or one day prior if no day of data were available, are used in this analysis to ensure only smoke plumes were sampled in the study. The lidar ratio remains relatively constant at all values of VDR retrieved for non-spherical smoke. Overall, the mean VDR for non-spherical smoke used in this analysis is 0.15.

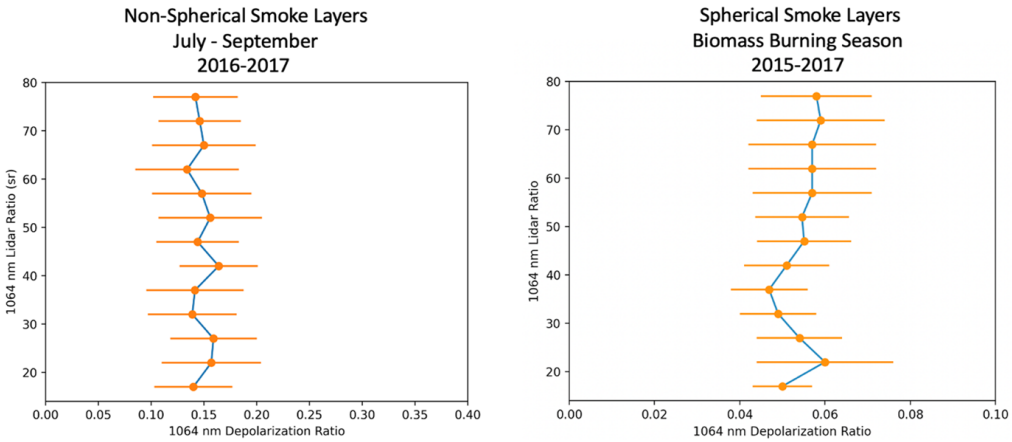

Figure 4. Layer-integrated 1064 nm constrained lidar ratio as a function of layer-integrated 1064 nm depolarization ratio for non-spherical (**left**) and spherical (**right**) smoke aerosol layers identified from CATS observations during the 2016–2017 (2015–2017 for spherical) biomass burning seasons are shown in blue with 1 standard deviation of the depolarization ratio shown in orange.

Figure 4 (right) shows the CATS 1064 nm constrained lidar ratio for spherical smoke aerosols as a function of VDR. The mean VDR for the spherical smoke aerosol layers is 0.05. Similarly to the non-spherical smoke plumes, there is no distinct trend between the lidar ratio and layer-integrated VDR for spherical smoke aerosol layers observed by CATS during the 2015–2017 biomass burning seasons. Therefore, Figure 4 shows that there is no statistically significant dependence of smoke plume lidar ratio on particle shape observed from CATS retrievals.

The same analysis described in the previous section was also conducted for CALIOP-observed smoke aerosol layers to see if the results are consistent between the two space-based lidars. Figure 5 (left) shows the CALIOP 532 nm opaque constrained lidar ratio as a function of the 532 nm layer-integrated particulate depolarization ratio $\pm$ 1 standard deviation for non-spherical smoke aerosol layers identified in the CALIOP data over southern Africa during July–September 2016–2017. As described previously, this time period was chosen to minimize dust contamination and align with operational AERONET stations within the domain. The mean value of the layer-integrated particulate depolarization ratio for the smoke layers presented in Figure 5 (left) is 0.12. Similarly to the results highlighted in Figure 4 (left), the CALIOP lidar ratio retrievals show no significant trend with layer-integrated particulate depolarization ratio over this domain and analysis period. Additionally, Figure 5 (right) shows the CALIOP opaque constrained lidar ratio as a function of layer-integrated depolarization ratio $\pm$ 1 standard deviation for spherical smoke layers identified is this analysis. The mean value of layer-integrated depolarization for these spherical smoke layers is 0.03. However, no clear trend is evident between the variables analyzed in this Figure. The results in Figure 5 show no statistically significant relationship between lidar ratio and depolarization ratio for the smoke layers observed by CALIOP in this analysis. These results align with the analysis of lidar ratio and 1064 nm VDR in the CATS data as well (Figure 4).

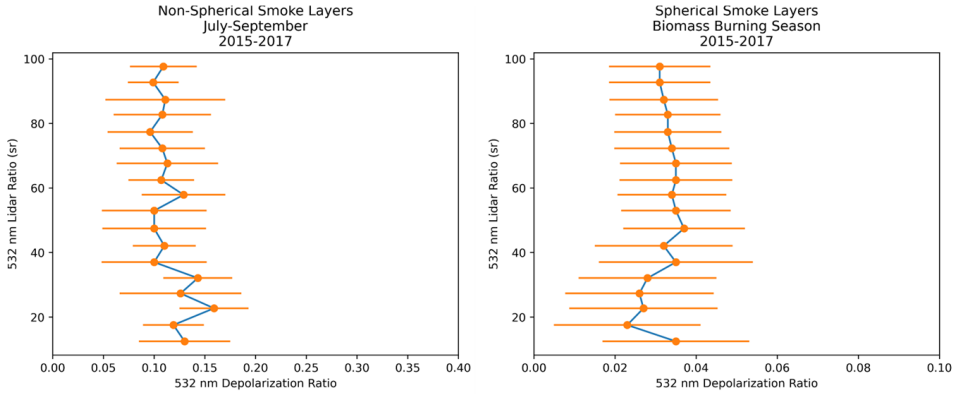

Figure 5. Layer-integrated 532 nm constrained lidar ratio as a function of layer-integrated 532 nm depolarization ratio for non-spherical (**left**) and spherical (**right**) smoke aerosol layers identified from CALIOP observations during the 2016–2017 (2015–2017 for spherical) biomass burning seasons are shown in blue with 1 standard deviation of the depolarization ratio shown in orange.

3.3. Dependence of Smoke Aerosol Lidar Ratio on Relative Humidity Using CATS and CALIOP Observations

An analysis was also conducted to explore the linkage between relative humidity and lidar ratio values as retrieved by the AERONET constrained and aerosol above-cloud constrained lidar ratio calculations for both CATS and CALIOP. Figure 6 (left) shows the retrieved layer-average lidar ratio for non-spherical smoke aerosols from both constrained methods described previously as a function of layer-averaged relative humidity derived from MERRA-2 provided in the CATS data products. Trends are shown for each year individually (2016 in orange; 2017 in green) and the two-year mean (black line). Gray shading indicates ± 1 standard deviation of the lidar ratio for these constrained calculations and a line of best fit is shown in red. In addition to the criteria discussed above, only smoke aerosol layers with CATS 1064 nm AOD > 0.1 were used in this analysis to filter out retrievals of background aerosol. However, note that this restraint may filter out tenuous smoke layers over the region. There is large variability in the mean layer lidar ratio values across the range of layer-integrated relative humidity values in this analysis for non-spherical smoke aerosols, likely due to the small number of observations. Overall, there is weak correlation (correlation coefficient of 0.33) and a coefficient of determination (r^2) value of 0.11 between non-spherical smoke layer lidar ratio and layer-averaged relative humidity in the CATS observations of biomass burning smoke plumes.

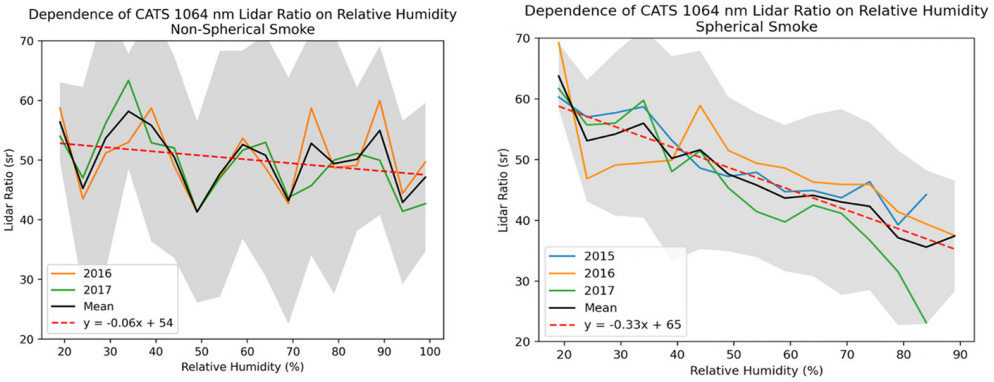

Figure 6. Layer-integrated 1064 nm constrained lidar ratio as a function of layer-integrated relative humidity observed by CATS for non-spherical (**left**) and spherical (**right**) smoke aerosol layers during 2015 (blue), 2016 (orange) and 2017 (green) and mean of all years (black). Gray shading represents ± 1 standard deviation of the lidar ratio. A line of best fit is also shown (red dashed).

The 1064 nm layer-average constrained lidar ratio with respect to the CATS layer-averaged relative humidity for spherical smoke plumes is shown in Figure 6 (right) for three years of CATS data (2015 in blue; 2016 in orange; 2017 in green) and the three-year mean (black line). Gray shading indicates ± 1 standard deviation of the layer lidar ratio and the line of best fit is shown in red. A clear trend in lidar ratio for spherical smoke plumes is evident. As layer relative humidity increases from 20 to 90%, there is a decrease in the mean lidar ratio from 65 sr to 43 sr. The r^2 for spherical smoke lidar ratio and layer-averaged relative humidity for the three years of CATS observations was found to be 0.91, and a correlation coefficient (r) of ~0.95 was found, indicating a significant linear relationship between the lidar ratio and layer-averaged relative humidity for spherical smoke aerosol particles. This result is in a sharp contrast with non-spherical smoke aerosol particles, for which no linear relationship was found between lidar ratio and relative humidity. The best fit line and corresponding equation in Figure 6 (right) provide a possible pathway to more accurately parameterize the lidar ratio in backscatter lidar extinction retrievals.

This analysis was repeated, substituting the CATS retrievals with CALIOP 532 nm opaque constrained and AERONET constrained lidar ratios and layer-averaged relative humidity derived from MERRA-2 provided in the CALIPSO data products. The results for non-spherical smoke layers are highlighted in Figure 7 (left) showing trends for each year individually (2016 in orange; 2017 in green) and the two-year mean (black line). Gray shading indicates ± 1 standard deviation of the lidar ratio for these constrained calculations and a line of best fit is shown in red. Large uncertainty is shown by the wide range in standard deviation for these variables and no clear trend is present for the dependence of non-smoke aerosol lidar ratio on relative humidity. Overall, there is an r of 0.34 and an r^2 value of 0.12 between the non-spherical smoke layer lidar ratio and layer-averaged relative humidity in the CALIOP observations of biomass burning smoke plumes.

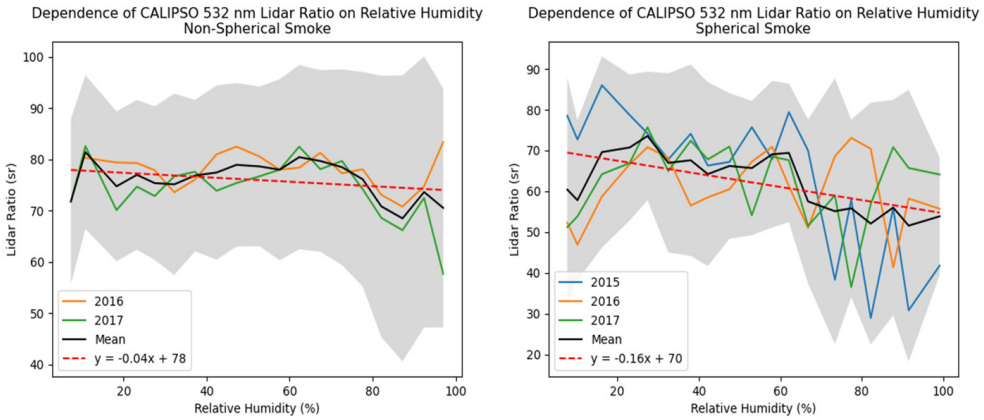

Figure 7. Layer-integrated 532 nm constrained lidar ratio as a function of layer-integrated relative humidity observed by CALIOP for non-spherical (**left**) and spherical (**right**) smoke aerosol layers during 2015 (blue), 2016 (orange) and 2017 (green) and mean of all years (black). Gray shading represents ± 1 standard deviation of the lidar ratio. A line of best fit is also shown (red dashed).

Similarly, the changes in the 532 nm layer constrained lidar ratio with respect to the CALIOP layer-averaged relative humidity for spherical smoke plumes are shown in Figure 7 (right) for three years of CALIOP data (2015 in blue; 2016 in orange; 2017 in green) and the three-year mean (black line). Again, gray shading indicates ± 1 standard deviation of the layer lidar ratio and the line of best fit is shown in red. A decreasing lidar ratio with increasing relative humidity is evident in the CALIOP analysis; however, this trend is less pronounced than in Figure 6 (right) of the CATS spherical smoke observations. As the layer relative humidity increases from ~10 to 90%, the lidar ratio only decreases from 70 to 60 sr.

The r^2 and r for the spherical smoke lidar ratio and layer-averaged relative humidity for the three years of CALIOP observations were found to be 0.41 and 0.64, respectively.

4. Discussion

Compositional differences have been noted in smoke particles from differing fire regimes (i.e., flaming or smoldering) [52–55]. For example, non-spherical smoke particles from flaming combustion have been found to contain higher concentrations of black carbon than their spherical smoke counterparts [39,56]. Furthermore, Midzak et al. (2023) [17] found that dry regions of Africa with low soil moisture produce non-spherical smoke aerosols, which is due to the higher temperature flaming combustion fires that occur in these regions. Therefore, we hypothesize that the trends in lidar ratio as a function of relative humidity can likely be explained due to the smoke particle compositional differences in spherical and non-spherical smoke layers.

Fresh, non-spherical smoke particles, which are predominantly black carbon, have been noted to exhibit hydrophobic properties [25,57]. As such, the presence of water vapor does not greatly impact the hydrophobic soot particle growth, and the smoke layer optical properties remain relatively constant [58]. In contrast, studies such as Gialitaki et al. (2020) [59] and Wu et al. (2016) [60] note that spherical smoke particles comprise inorganic, hydrophilic coatings that include water-soluble compounds. Kar et al. (2018) [25] found that the enhanced hygroscopicity of spherical smoke particles worked to increase water uptake and promote particle swelling, especially as the plumes traveled closer to the coast of Africa and over the ocean. These swelled particles then exhibit a reduction in their light absorption capabilities (Müller et al., 2007) [6], thus decreasing the lidar ratio as relative humidity increases (Midzak et al., 2023) [17]. This is consistent with the results shown in Figure 6 (right) and, to a lesser degree, Figure 7 (right). The lidar ratio is a complex parameter that depends on the size, absorption properties and chemical composition of particles [6], which is inherently dependent on the smoke source region, available moisture and type of fire from which the smoke plumes are produced [61]. Because the lidar ratio remains one of the largest sources of uncertainty for lidar extinction retrievals, efforts must be made to improve aerosol classification and aerosol lidar ratio retrievals.

The dependence of lidar ratio on relative humidity has been explored previously using theoretical analyses and lidar retrievals. Most recently, Eggers et al. (2024) [62] studied biomass burning transported over Arctic regions and noted the complexities involved in lidar ratio determination, including the particle size, shape and refractive index. They found a slight decrease in 355 and 532 nm lidar ratio as relative humidity increased from ~20–80% but stressed the complex nature of lidar ratio variability. Additionally, Chipade and Pandya (2023) [63] presented a physics-based theoretical approach to estimate lidar ratio values for CALIPSO aerosol models. The authors used Optical Properties of Aerosols and Clouds (OPAC) aerosol models to study the effects of relative humidity on aerosol optical properties. Their results showed a decrease in lidar ratio with increasing relative humidity at 1064 nm and, to a lesser extent, 532 nm for continental and maritime aerosols. This trend was attributed to the hygroscopic nature of the particles. As relative humidity increased, the imaginary part of the refractive index, and thus absorption, decreased. Thus, the extinction coefficient increased at a rate less than or equal to the rate of the backscatter coefficient increasing [63]. Soot and water-soluble aerosols near the coast and in the planetary boundary layer over oceans were examined by Ackerman (1998) [64]. A decrease in lidar ratio with relative humidity was found to be a function of wavelength, with 1064 nm showing the largest variability in lidar ratio. These studies align with the results of this analysis; however, other studies, such as Anderson et al. (2000) [65], Zhao et al. (2017) [66],

and Dawson et al. (2020) [67], highlight findings of increased lidar ratio with relative humidity due to increased scattering enhancement factors. Overall, each of these studies highlight the complexities of accurate lidar ratio retrievals for complex aerosol types such as smoke particles.

The vertical profiles of extinction coefficient for a smoke plume over Angola in southern Africa (−16.7°/12.3°) observed by CATS on 7 August 2016 at 01:57:42 UTC are highlighted in Figure 8 using multiple techniques. The extinction coefficients using a collocated AERONET AOD retrieval as a constraint, as described above (orange line), are considered the truth for this case. Two lidar ratio parameterizations are also included: (1) the standard CATS smoke aerosol default lidar ratio selection with a value of 40 sr (blue line) and (2) a lidar ratio value selected by the line of best fit according to the relative humidity of the plume from Figure 6 (green line). It is evident that a default lidar ratio selection method (blue) results in the largest values of extinction for the entire vertical extent of the smoke plume, which stretches from 2 km to 4.5 km in altitude. The extinction calculated using a value based on the plume relative humidity (green) is the lowest of all three profiles. Figure 8 indicates that, in the case of this smoke aerosol layer, a default value of 40 sr for the lidar ratio results in a high bias of the extinction coefficient and, thus, the AOD of the plume. These results also indicate that a lidar ratio constraint based on the relative humidity line of best fit from Figure 6 or 7 (right) would result in a more accurate extinction retrieval than assigning a default lidar ratio based on aerosol type. A look-up table approach based on relative humidity for assigning lidar ratio can be considered for future backscatter lidar algorithms. As others such as Zhao et al. (2017) [66] and Midzak et al. (2022) [26] have noted, a dynamic method for lidar ratio retrieval may help reduce large uncertainties in backscatter lidar extinction retrievals that result from inaccuracies in lidar ratio values when only a static value is considered.

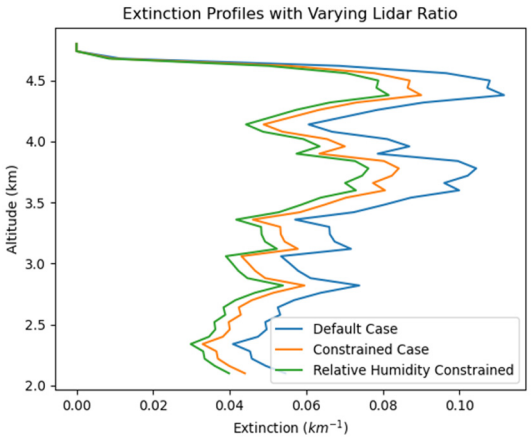

Figure 8. Extinction profiles through a smoke plume observed by CATS on 7 August 2016 resulting from a default lidar ratio assignment (blue), a constrained lidar ratio (orange) and a lidar ratio assigned based on the layer relative humidity (green).

5. Conclusions

This study builds on the work of Midzak et al. (2023) [17], who present an analysis of non-spherical smoke aerosols observed by the CATS lidar from African biomass burning. The frequency and spatial distributions of spherical and non-spherical smoke aerosol layers observed by CALIOP over Africa during the biomass burning season 2015–2017 are presented here and align well with the results of Midzak et al. (2023) [17]. Non-spherical smoke layers are identified using a 532 nm layer-integrated particulate depolarization ratio threshold > 0.075 and are most frequently observed in dryer regions of southern Africa. In contrast, spherical smoke aerosols with layer-integrated particulate depolarization ratio

values <0.075 are closer to the equator in moist biomes. Assumptions about smoke particle sphericity may lead to misclassifications of smoke aerosol layers due to the threshold-based nature of aerosol classification schemes implemented by backscatter lidars such as CATS and CALIOP. Inaccuracies in layer typing may result in uncertainties in aerosol extinction retrievals and the AOD. No clear trend was found between the smoke aerosol lidar ratio and layer-averaged depolarization ratio; however, this analysis shows an inverse trend in spherical smoke lidar ratio and layer-averaged relative humidity. These trends are likely due to the smoke particle composition as hydrophobic non-spherical smoke optical properties remain relatively stable throughout all relative humidity values observed. However, hygroscopic spherical smoke particles uptake water [25], and their scattering and extinction properties evolve with changes in relative humidity [6,63]. These results suggest that a dynamic lidar ratio may be implemented based on layer relative humidity for spherical smoke to reduce uncertainties in smoke aerosol extinction retrievals of future backscatter lidars.

Author Contributions: N.M., J.E.Y. and J.Z. designed the study. N.M. implemented the experiment, drafted the original manuscript and created visualizations. J.E.Y. and J.Z. provided valuable comments to the study. J.E.Y., J.Z. and N.M. edited the manuscript. All authors have read and agreed to the published version of the manuscript.

Funding: JZ was partially funded by the NASA grants 80NSSC20K1748 and 80NSSC24K1180.

Data Availability Statement: All CATS data products used in this paper and documents such as the data products catalog, release notes and algorithm theoretical basis documents (ATBDs) are available at the CATS website (https://cats.gsfc.nasa.gov). All CATS and CALIOP data are available at the NASA Atmospheric Science Data Center (https://asdc.larc.nasa.gov/).

Acknowledgments: This research was supported by an appointment to the NASA Postdoctoral Program at NASA Goddard Space Flight Center, administered by Oak Ridge Associated Universities under contracts with NASA.

Conflicts of Interest: The authors declare no conflicts of interest.

References

1. Bond, T.C.; Doherty, S.J.; Fahey, D.W.; Forster, P.M.; Berntsen, T.; DeAngelo, B.J.; Flanner, M.G.; Ghan, S.; Kärcher, B.; Koch, D.; et al. Bounding the role of black carbon in the climate system: A scientific assessment. *J. Geophys. Res. Atmos.* **2013**, *118*, 5380–5552. [CrossRef]
2. Markowicz, K.M.; Flatau, P.J.; Kardas, A.E.; Remiszewska, J.; Stelmaszczyk, K.; Woeste, L. Ceilometer retrieval of the boundary layer vertical aerosol extinction structure. *J. Atmos. Ocean. Technol.* **2008**, *25*, 928–944. [CrossRef]
3. Spinhirne, J.D.; Reagan, J.A.; Herman, B.M. Vertical distribution of aerosol extinction cross section and inference of aerosol imaginary index in the troposphere by lidar technique. *J. Appl. Meteorol. Climatol.* **1980**, *19*, 426–438. [CrossRef]
4. Klett, J.D. Stable analytical inversion solution for processing lidar returns. *Appl. Opt.* **1981**, *20*, 211–220. [CrossRef] [PubMed]
5. Fernald, F.G. Analysis of atmospheric lidar observations: Some comments. *Appl. Opt.* **1984**, *23*, 652–653. [CrossRef] [PubMed]
6. Müller, D.; Ansmann, A.; Mattis, I.; Tesche, M.; Wandinger, U.; Althausen, D.; Pisani, G. Aerosol-type-dependent lidar ratios observed with Raman lidar. *J. Geophys. Res. Atmos.* **2007**, *112*, 1–11. [CrossRef]
7. Pauly, R.M.; Yorks, J.E.; Hlavka, D.L.; McGill, M.J.; Amiridis, V.; Palm, S.P.; Rodier, S.D.; Vaughan, M.A.; Selmer, P.A.; Kupchock, A.W.; et al. Cloud-Aerosol Transport System (CATS) 1064 nm calibration and validation. *Atmos. Meas. Tech.* **2019**, *12*, 6241–6258. [CrossRef] [PubMed]
8. Lee, L.; Zhang, J.; Reid, J.S.; Yorks, J.E. Investigation of CATS aerosol products and application toward global diurnal variation of aerosols. *Atmos. Chem. Phys.* **2019**, *19*, 12687–12707. [CrossRef]
9. Schuster, G.L.; Vaughan, M.; MacDonnell, D.; Su, W.; Winker, D.; Dubovik, O.; Lapyonok, T.; Trepte, C. Comparison of CALIPSO aerosol optical depth retrievals to AERONET measurements, and a climatology for the lidar ratio of dust. *Atmos. Chem. Phys.* **2012**, *12*, 7431–7452. [CrossRef]

10. Rogers, R.R.; Vaughan, M.A.; Hostetler, C.A.; Burton, S.P.; Ferrare, R.A.; Young, S.A.; Hair, J.W.; Obland, M.D.; Harper, D.B.; Cook, A.L.; et al. Looking through the haze: Evaluating the CALIPSO level 2 aerosol optical depth using airborne high spectral resolution lidar data. *Atmos. Meas. Tech.* **2014**, *7*, 4317–4340. [CrossRef]
11. Palm, S.; Hart, W.; Hlavka, D.; Welton, E.J.; Mahesh, A.; Spinhirne, J. *GLAS Atmospheric Data Products. Geoscience Laser Altimeter System (GLAS): Algorithm Theoretical Basis Document Version 4.2*; NASA Goddard Space Flight Center: Greenbelt, MD, USA, 2002.
12. Omar, A.H.; Winker, D.M.; Vaughan, M.A.; Hu, Y.; Trepte, C.R.; Ferrare, R.A.; Lee, K.-P.; Hostetler, C.A.; Kittaka, C.; Rogers, R.R.; et al. The CALIPSO automated aerosol classification and lidar ratio selection algorithm. *J. Atmos. Ocean. Technol.* **2009**, *26*, 1994–2014. [CrossRef]
13. Kim, M.-H.; Omar, A.H.; Tackett, J.L.; Vaughan, M.A.; Winker, D.M.; Trepte, C.R.; Hu, Y.; Liu, Z.; Poole, L.R.; Pitts, M.C.; et al. The CALIPSO version 4 automated aerosol classification and lidar ratio selection algorithm. *Atmos. Meas. Tech.* **2018**, *11*, 6107–6135. [CrossRef] [PubMed]
14. Nowottnick, E.P.; Christian, K.E.; Yorks, J.E.; McGill, M.J.; Midzak, N.; Selmer, P.A.; Lu, Z.; Wang, J.; Salinas, S.V. Aerosol Detection from the Cloud–Aerosol Transport System on the International Space Station: Algorithm Overview and Implications for Diurnal Sampling. *Atmosphere* **2022**, *13*, 1439. [CrossRef]
15. Burton, S.P.; Hair, J.W.; Kahnert, M.; Ferrare, R.A.; Hostetler, C.A.; Cook, A.L.; Harper, D.B.; Berkoff, T.A.; Seaman, S.T.; Collins, J.E.; et al. Observations of the spectral dependence of linear particle depolarization ratio of aerosols using NASA Langley airborne High Spectral Resolution Lidar. *Atmos. Chem. Phys.* **2015**, *15*, 13453–13473. [CrossRef]
16. Martins, J.V.; Hobbs, P.V.; Weiss, R.E.; Artaxo, P. Sphericity and morphology of smoke particles from biomass burning in Brazil. *J. Geophys. Res. Atmos.* **1998**, *103*, 32051–32057. [CrossRef]
17. Midzak, N.; Yorks, J.E.; Zhang, J.; Nowottnick, E.P. An investigation of non-spherical smoke particles using CATS lidar. *J. Geophys. Res. Atmos.* **2023**, *128*, e2023D038805. [CrossRef]
18. Liu, L.; Mishchenko, M.I. Scattering and radiative properties of morphologically complex carbonaceous aerosols: A systematic modeling study. *Remote Sens.* **2018**, *10*, 1634. [CrossRef]
19. Mishchenko, M.I.; Dlugach, J.M.; Liu, L. Linear depolarization of lidar returns by aged smoke particles. *Appl. Opt.* **2016**, *55*, 9968–9973. [CrossRef]
20. Sorensen, C.M. Light scattering by fractal aggregates: A review. *Aerosol Sci. Technol.* **2001**, *35*, 648–687. [CrossRef]
21. Haarig, M.; Ansmann, A.; Baars, H.; Jimenez, C.; Veselovskii, I.; Engelmann, R.; Althausen, D. Depolarization and lidar ratios at 355, 532, and 1064 nm and microphysical properties of aged tropospheric and stratospheric Canadian wildfire smoke. *Atmos. Chem. Phys.* **2018**, *18*, 11847–11861. [CrossRef]
22. Ansmann, A.; Baars, H.; Chudnovsky, A.; Mattis, I.; Veselovskii, I.; Haarig, M.; Seifert, P.; Engelmann, R.; Wandinger, U. Extreme levels of Canadian wildfire smoke in the stratosphere over central Europe on 21–22 August 2017. *Atmos. Chem. Phys.* **2018**, *18*, 11831–11845. [CrossRef]
23. Khaykin, S.M.; Godin-Beekmann, S.; Keckhut, P.; Hauchecorne, A.; Jumelet, J.; Vernier, J.-P.; Bourassa, A.; Degenstein, D.A.; Rieger, L.A.; Bingen, C.; et al. Variability and evolution of the midlatitude stratospheric aerosol budget from 22 years of ground-based lidar and satellite observations. *Atmos. Chem. Phys.* **2017**, *17*, 1829–1845. [CrossRef]
24. He, Y.; Jing, D.; Yin, Z.; Ohneiser, K.; Yi, F. Long-term (2010–2021) lidar observations of stratospheric aerosols in Wuhan, China. *Atmos. Chem. Phys.* **2024**, *24*, 11431–11450. [CrossRef]
25. Kar, J.; Vaughan, M.; Tackett, J.; Liu, Z.; Omar, A.; Rodier, S.; Trepte, C.; Lucker, P. Swelling of Transported Smoke from Savanna fires over the Southeast Atlantic Ocean. *Remote Sens. Environ.* **2018**, *211*, 105–111. [CrossRef]
26. Midzak, N.; Yorks, J.E.; Zhang, J.; Limbacher, J.A.; Kalashnikova, O.V.; Garay, M.J. Constrained retrievals of aerosol optical properties using combined lidar and imager measurements during the FIREX-AQ campaign. *Front. Remote Sens.* **2022**, *3*, 818605. [CrossRef]
27. Hu, Y.; Vaughan, M.; Liu, Z.; Powell, K.; Rodier, S. Retrieving optical depths and lidar ratios for transparent layers above opaque water clouds from CALIPSO lidar measurements. *IEEE Geosci. Remote Sens. Lett.* **2007**, *4*, 523–526. [CrossRef]
28. Yorks, J.E.; Palm, S.P.; Hlavka, D.L.; McGill, M.J.; Nowottnick, E.; Selmer, P.; Hart, W.D. The Cloud-Aerosol Transport System (CATS) Algorithm Theoretical Basis Document. 2015. Available online: http://cats.gsfc.nasa.gov/media/docs/CATS_ATBD.pdf (accessed on 11 January 2025).
29. McGill, M.J.; Yorks, J.E.; Scott, V.S.; Kupchock, A.W.; Selmer, P.A. The cloud-aerosol transport system (CATS): A technology demonstration on the international space station. In *Lidar Remote Sensing for Environmental Monitoring XV, Proceedings of the SPIE Optical Engineering + Applications 2015, San Diego, CA, USA, 9–13 August 2015*; SPIE: Greenbelt, MD, USA, 2015; Volume 9612, pp. 34–39.
30. Yorks, J.E.; Selmer, P.A.; Kupchock, A.; Nowottnick, E.P.; Christian, K.E.; Rusinek, D.; Dacic, N.; McGill, M.J. Aerosol and Cloud Detection Using Machine Learning Algorithms and Space-Based Lidar Data. *Atmosphere* **2021**, *12*, 606. [CrossRef]

31. Luo, B.; Minnett, P.J.; Szczodrak, M.; Nalli, N.R.; Morris, V.R. Accuracy assessment of MERRA-2 and ERA-Interim sea surface temperature, air temperature, and humidity profiles over the atlantic ocean using AEROSE measurements. *J. Clim.* **2020**, *33*, 6889–6909. [CrossRef]
32. Winker, D.M.; Pelon, J.; Coakley, J.A., Jr.; Ackerman, S.A.; Charlson, R.J.; Colarco, P.R.; Flamant, P.; Fu, Q.; Hoff, R.M.; Kittaka, C.; et al. The CALIPSO mission: A global 3D view of aerosols and clouds. *Bull. Am. Meteorol. Soc.* **2010**, *91*, 1211–1230. [CrossRef]
33. Adebiyi, A.A.; Zuidema, P.; Abel, S.J. The Convolution of Dynamics and Moisture with the Presence of Shortwave Absorbing Aerosols over the Southeast Atlantic. *J. Clim.* **2015**, *28*, 1997–2024. [CrossRef]
34. Kalnay, E.; Kanamitsu, M.; Kistler, R.; Collins, W.; Deaven, D.; Gandin, L.; Iredell, M.; Saha, S.; White, G.; Woollen, J.; et al. The NCEP/NCAR 40-year reanalysis project. *Bull. Am. Meteorol. Soc.* **1996**, *77*, 437–472. [CrossRef]
35. Holben, B.N.; Eck, T.F.; Slutsker, I.; Tanré, D.; Buis, J.P.; Setzer, A.; Vermote, E.; Reagan, J.A.; Kaufman, Y.J.; Nakajima, T.; et al. AERONET—A federated instrument network and data archive for aerosol characterization. *Remote Sens. Environ.* **1998**, *66*, 1–16. [CrossRef]
36. Eck, T.F.; Holben, B.N.; Reid, J.S.; Dubovik, O.; Smirnov, A.; O'Neill, N.T.; Slutsker, I.; Kinne, S. Wavelength dependence of the optical depth of biomass burning, urban, and desert dust aerosols. *J. Geophys. Res. Atmos.* **1999**, *104*, 31333–31349.
37. Holben, B.N.; Kaufman, Y.J.; Setzer, A.W.; Tanre, D.D.; Ward, D.E. Optical properties of aerosol emissions from biomass burning in the tropics, BASE-A. In *Global Biomass Burning: Atmospheric, Climatic, and Biospheric Implications*; MIT Press: Cambridge, MA, USA, 1991; pp. 403–411.
38. Kaufman, Y.J.; Setzer, A.; Ward, D.; Tanre, D.; Holben, B.N.; Menzel, P.; Pereira, M.C.; Rasmussen, R. Biomass burning airborne and spaceborne experiment in the Amazonas (BASE-A). *J. Geophys. Res. Atmos.* **1992**, *97*, 14581–14599. [CrossRef]
39. Reid, J.S.; Eck, T.F.; Christopher, S.A.; Hobbs, P.V.; Holben, B. Use of the Ångstrom exponent to estimate the variability of optical and physical properties of aging smoke particles in Brazil. *J. Geophys. Res. Atmos.* **1999**, *104*, 27473–27489.
40. Tackett, J.L.; Kar, J.; Vaughan, M.A.; Getzewich, B.J.; Kim, M.-H.; Vernier, J.-P.; Omar, A.H.; Magill, B.E.; Pitts, M.C.; Winker, D.M. The CALIPSO version 4.5 stratospheric aerosol subtyping algorithm. *Atmos. Meas. Tech.* **2023**, *16*, 745–768. [CrossRef]
41. Yorks, J.E.; Hlavka, D.L.; Hart, W.D.; McGill, M.J. Statistics of cloud optical properties from airborne lidar measurements. *J. Atmos. Ocean. Technol.* **2011**, *28*, 869–883. [CrossRef]
42. Liu, Z.; Winker, D.; Omar, A.; Vaughan, M.; Kar, J.; Trepte, C.; Hu, Y.; Schuster, G. Evaluation of CALIOP 532 nm aerosol optical depth over opaque water clouds. *Atmos. Chem. Phys.* **2015**, *15*, 1265–1288. [CrossRef]
43. Fernald, F.G.; Herman, B.M.; Reagan, J.A. Determination of aerosol height distributions by lidar. *J. Appl. Meteorol. Climatol.* **1972**, *11*, 482–489. [CrossRef]
44. Welton, E.J.; Voss, K.J.; Gordon, H.R.; Maring, H.; Smirnov, A.; Holben, B.; Schmid, B.; Livingston, J.M.; Russell, P.B.; Durkee, P.A.; et al. Ground-based lidar measurements of aerosols during ACE-2: Instrument description, results, and comparisons with other ground-based and airborne measurements. *Tellus* **2000**, *52*, 636–651. [CrossRef]
45. Burton, S.P.; Ferrare, R.A.; Hostetler, C.A.; Hair, J.W.; Kittaka, C.; Vaughan, M.A.; Obland, M.D.; Rogers, R.R.; Cook, A.L.; Harper, D.B.; et al. Using airborne high spectral resolution lidar data to evaluate combined active plus passive retrievals of aerosol extinction profiles. *J. Geophys. Res. Atmos.* **2010**, *115*, D00H15. [CrossRef]
46. McGill, M.J.; Hlavka, D.L.; Hart, W.D.; Welton, E.J.; Campbell, J.R. Airborne lidar measurements of aerosol optical properties during SAFARI-2000. *J. Geophys. Res. Atmos.* **2003**, *108*, 8493. [CrossRef]
47. Swap, R.J.; Annegarn, H.J.; Cook, B.; Desanker, P.; Djolov, G.; Doddridge, B.; Dowty, P. *Southern African Regional Science Initiative: Safari 2000: Science Plan*; The University of Virginia: Charlottesville, VA, USA, 1999.
48. Zuidema, P.; Sedlacek, A.J.; Flynn, C.; Springston, S.; Delgadillo, R.; Zhang, J.; Aiken, A.C.; Koontz, A.; Muradyan, P. The Ascension Island boundary layer in the remote Southeast Atlantic is often smoky. *Geophys. Res. Lett.* **2018**, *45*, 4456–4465. [CrossRef]
49. Swap, R.J.; Annegarn, H.J.; Suttles, J.T.; Haywood, J.; Helmlinger, M.C.; Hely, C.; Hobbs, P.V.; Holben, B.N.; Ji, J.; King, M.D.; et al. The Southern African Regional Science Initiative (SAFARI 2000): Overview of the dry season field campaign. *S. Afr. J. Sci.* **2002**, *98*, 125–130.
50. Zuidema, P.; Redemann, J.; Haywood, J.; Wood, R.; Piketh, S.; Hipondoka, M.; Formenti, P. Smoke and Clouds above the Southeast Atlantic: Upcoming Field Campaigns Probe Absorbing Aerosol's Impact on Climate. *Bull. Am. Meteorol. Soc.* **2016**, *97*, 1131–1135. [CrossRef]
51. Matichuk, R.I.; Colarco, P.R.; Smith, J.A.; Toon, O.B. Modeling the transport and optical properties of smoke aerosols from African savanna fires during the Southern African Regional Science Initiative campaign (SAFARI 2000). *J. Geophys. Res. Atmos.* **2007**, *112*, D08203. [CrossRef]
52. Hobbs, P.V. *Summary of Types of Data Collected on the University of Washington's Convair C131-A aircraft in the Smoke, Clouds, and Radiation-Brazil (SCAR-B) Field Study from 17 August–20 September 1995*; University of Washington: Seattle, WA, USA, 1996.
53. Pósfai, M.; Simonics, R.; Li, J.; Hobbs, P.V.; Buseck, P.R. Individual aerosol particles from biomass burning in southern Africa: 1. Compositions and size distributions of carbonaceous particles. *J. Geophys. Res. Atmos.* **2003**, *108*, 8483. [CrossRef]

54. Freitas, S.R.; Longo, K.M.; Chatfield, R.; Latham, D.; Dias, M.A.F.S.; Andreae, M.O.; Prins, E.; Santos, J.C.; Gielow, R.; Carvalho, J.A., Jr. Including the sub-grid scale plume rise of vegetation fires in low resolution atmospheric transport models. *Atmos. Chem. Phys.* **2007**, *7*, 3385–3398. [CrossRef]
55. Darbyshire, E.; Morgan, W.T.; Allan, J.D.; Liu, D.; Flynn, M.J.; Dorsey, J.R.; O'Shea, S.J.; Lowe, D.; Szpek, K.; Marenco, F.; et al. The vertical distribution of biomass burning pollution over tropical South America from aircraft in situ measurements during SAMBBA. *Atmos. Chem. Phys.* **2019**, *19*, 5771–5790. [CrossRef]
56. Bond, T.C.; Bergstrom, R.W. Light absorption by carbonaceous particles: An Investigative review. *Aerosol Sci. Technol.* **2006**, *40*, 27–67. [CrossRef]
57. Martins, J.V.; Artaxo, P.; Liousse, C.; Reid, J.S.; Hobbs, P.V.; Kaufman, Y.J. Effects of black carbon content, particle size, and mixing on light absorption by aerosols from biomass burning in Brazil. *J. Geophys. Res. Atmos.* **1998**, *103*, 32041–32050. [CrossRef]
58. Mikhailov, E.F.; Vlasenko, S.S.; Podgorny, I.A.; Ramanathan, V.; Corrigan, C.E. Optical properties of soot–water drop agglomerates: An experimental study. *J. Geophys. Res. Atmos.* **2006**, *111*, D07209. [CrossRef]
59. Gialitaki, A.; Tsekeri, A.; Amiridis, V.; Ceolato, R.; Paulien, L.; Kampouri, A.; Gkikas, A.; Solomos, S.; Marinou, E.; Haarig, M.; et al. Is the near-spherical shape the new black for smoke? *Atmos. Chem. Phys. Discuss.* **2020**, *20*, 14005–14021. [CrossRef]
60. Wu, Z.J.; Zheng, J.; Shang, D.J.; Du, Z.F.; Wu, Y.S.; Zeng, L.M.; Wiedensohler, A.; Hu, M. Particle hygroscopicity and its link to chemical composition in the urban atmosphere of Beijing, China, during summertime. *Atmos. Chem. Phys.* **2016**, *16*, 1123–1138. [CrossRef]
61. Nicolae, D.; Nemuc, A.; Müller, D.; Talianu, C.; Vasilescu, J.; Belegante, L.; Kolgotin, A. Characterization of fresh and aged biomass burning events using multiwavelength Raman lidar and mass spectrometry. *J. Geophys. Res. Atmos.* **2013**, *118*, 2956–2965. [CrossRef]
62. Eggers, N.; Graßl, S.; Ritter, C. Assessment of Hygroscopic Behavior of Arctic Aerosol by Contemporary Lidar and Radiosonde Observations. *Remote Sens.* **2024**, *16*, 3087. [CrossRef]
63. Chipade, R.A.; Pandya, M.R. Theoretical derivation of aerosol lidar ratio using Mie theory for CALIOP-CALIPSO and OPAC aerosol models. *Atmos. Meas. Tech.* **2023**, *16*, 5443–5459. [CrossRef]
64. Ackermann, J. The extinction-to-backscatter ratio of tropospheric aerosol: A numerical study. *J. Atmos. Ocean. Technol.* **1998**, *15*, 1043–1050. [CrossRef]
65. Anderson, T.L.; Masonis, S.J.; Covert, D.S.; Charlson, R.J.; Rood, M.J. In situ measurement of the aerosol extinction-to-backscatter ratio at a polluted continental site. *J. Geophys. Res. Atmos.* **2000**, *105*, 26907–26915. [CrossRef]
66. Zhao, G.; Zhao, C.; Kuang, Y.; Tao, J.; Tan, W.; Bian, Y.; Li, J.; Li, C. Impact of aerosol hygroscopic growth on retrieving aerosol extinction coefficient profiles from elastic-backscatter lidar signals. *Atmos. Chem. Phys.* **2017**, *17*, 12133–12143. [CrossRef]
67. Dawson, K.W.; Ferrare, R.A.; Moore, R.H.; Clayton, M.B.; Thorsen, T.J.; Eloranta, E.W. Ambient aerosol hygroscopic growth from combined Raman lidar and HSRL. *J. Geophys. Res. Atmos.* **2020**, *125*, e2019JD031708zz. [CrossRef]